Tuneable Gradient Helmholtz-resonator-based Acoustic Metasurface for Acoustic Focusing

Kemeng Gong[1], Xiaofan Wang[1], Huajiang Ouyang[2], Jiliang Mo[1,a]

[1]*Tribology Research Institute, Southwest Jiaotong University, Chengdu 610031, China*

[2]*School of Engineering, University of Liverpool, Liverpool L69 3GH, UK*

[a]Author to whom correspondence should be addressed. Email: jlmo@swjtu.cn

Abstract

Conventional acoustic focusing requires an array of actuators or waveguides to form a complex wavefront, resulting in a high cost or bulky size. In this paper, an original gradient Helmholtz-resonator (HR)-based AMS is presented. The phase shift of AMS units can be precisely controlled over the full phase range and continuously tuned by varying the slit width. The transmission efficiency of the AMSs is relatively high, benefitting from the impedance matching. Several typical situations in acoustic focusing with different focusing parameters are realized by the designed AMSs. The results of the finite element method (FEM) demonstrate that moving the position of the focal point or changing the incident angle can be realized by tuning the slit width distribution. A further analysis indicates that the discrete resolution is considerably fine, as a result of the suitable deep-subwavelength parameters of the AMS and the high accuracy of the phase shift of each unit. The acoustic intensities at the focal point reach 12.3 to 17.6 times that of the incident plane wave, owing to the high transmission efficiency. Due to these significant advantages, the designed gradient HR-based AMS is able to offer a tuneable acoustic lens in medical sonography, localized heating, nondestructive flaw detection and particle trapping.

Keywords: acoustic metasurface, acoustic focusing, tuneability, Helmholtz resonator

1. Introduction

Acoustic focusing, as one of the essential ways of manipulating acoustic waves,

plays an important role not only in diagnostic medical sonography [1] and localized heating to treat tumours [2] in medical field, but also in nondestructive flaw detection techniques [3, 4] in engineering field. Numerous studies have investigated the ways to form an acoustic focusing beam for acoustic trapping [5] and acoustic tweezer [6] in recent years. Generally, utilizing piezoelectric transducers (PTs) to actively produce the required acoustic field and using a waveguide to passively converge an acoustic wave are conventional methods for realizing acoustic focusing. However, it is difficult to reduce the bulky size of these transducers and waveguides to a dimension smaller than the order of magnitude of the wavelength involved according to the classical acoustic theories [7, 8], which presents an obstacle for finer resolutions of acoustic focusing.

The last decade has witnessed intensive investigations of acoustic metasurface (AMS), which stems from the concept of electromagnetic metasurface such as optical metalens [9, 10]. The AMSs show the extraordinary properties in acoustic wave manipulation such as acoustic self-bending [11], cloaking [12, 13], focusing [14–16], perfect absorption [17, 18], sound insulation [19], anomalous refraction [20] and anomalous reflection [21–23]. Space-coiling AMSs have attracted much attention for acoustic wave manipulation from its good phase control ability and relatively wide response frequency bandwidth [14, 24]. Nevertheless, the intrinsic loss of space-coiling AMS will be quite large due to the curled and elongated channels, leading to a low transmittance coefficient [25–27]. Besides, membrane-type AMSs possess negative effective mass density and bulk modulus, which can readily realize a perfect acoustic absorber [28]. Helmholtz resonator (HR)-based AMSs, by virtue of the impedance matching, have enabled various acoustic manipulations in recent years [11, 16, 25]. The original concept of HR-based AMSs formed by periodical daisy-chained HRs linked on a duct was proposed by Li *et al* [11]. Benefitting from Fabry-Pérot resonance in the duct coupled with the resonance of HRs, this type of AMSs can achieve relatively high energy transmittance. Lan *et al* [16] designed a kind of HR-based AMSs which manipulates acoustic waves by providing desired discrete acoustic velocity distribution, and furthermore, by means of varying the slit width of each AMS unit.

Gradient metasurface was firstly proposed in the electromagnetic field [29, 30],

and then the concept of gradient was subsequently introduced to AMSs [16, 24]. Numerous researchers who study gradient AMSs rarely take into account the phase accuracy since the phase shift distribution (PSD) of the designed AMSs is an approximation of the ideal PSD to create required acoustic pressure field. In order to reduce the complexity and improve the feasibility of fabrication, a majority of the previous gradient AMSs contain only 4 to 8 subunits to cover the 0–2π phase range [11, 13, 18, 20, 25, 27], which also ensures considerably high transmission efficiency in the full phase range. However, these simplifications give rise to high systemic errors which can reach up to π/4–π/8 in an actual PSD due to the low number of subunits contained, causing the deviation of location of the acoustic focus and the distortion of the acoustic pressure field. On the other hand, some studies concentrate on the velocity distributions instead of the PSD when designing the acoustic pressure field of anomalous refraction, non-diffractive Bessel beam and focusing [15, 16]. Nevertheless, the widths of the AMSs in these studies are relatively small so that the full phase range ability is not concerned. Several recent studies in which the AMSs are designed with more gradient subunits, however, are still unable to cover the full phase range [14, 24].

Therefore, there is still an urgent demand for an acoustic lens to achieve acoustic focusing with the capabilities of (I) high transmission efficiency for gaining a high energy amplification factor at a focal point, (II) full phase controlling (2π range), (III) fine discrete resolution along the device and the direction of wave propagation, and (IV) tuneability for different focusing parameters, which means that focusing conditions can be controlled by adjusting a certain parameter of the lens instead of replacing the lens by another one. Existing acoustic metamaterials (AMMs) [31–35] and aforementioned AMSs do not have all of these capabilities.

In this study, an original gradient HR-based AMS for acoustic focusing which possesses the four capabilities mentioned above is proposed for the first time. Theoretical analysis and numerical simulation show that the phase shift of AMS units can be precisely controlled over the full phase range and continuously tuneable by means of varying the slit width. The AMS uses impedance matching in full phase range, which ensures the relatively high energy transmittance. Several typical acoustic

focusing situations with different focusing parameters are implemented by this type of AMSs with a certain distribution of slit width according to generalized Snell's law. The finite element method (FEM) is employed to simulate these focusing conditions. This type of AMS provides a new design methodology with excellent performance for acoustic focusing applications.

2. Results and discussions

First of all, it is necessary to clarify the structure design and properties of the AMS elementary unit. The unit of AMS is formed by a parallel one-dimensional daisy-chained slit with five HRs [cf. Fig. 1(a)] to shape the phase of the wavefront by varying the slit width d. The length a and width b of the HR cavity is 7.5 mm and 7.5 mm, respectively. The height h and width l of the HR neck is 1 mm and 4.4 mm, respectively. The length L of an HR of the AMS is 8.5 mm and the height H of an AMS unit is 9.5 mm. Besides, the thickness W of the AMS is subwavelength (44 mm). In the schematic diagram of the AMS shown in Fig. 1(b), sixty pieces of AMS units are arranged along the x-axis, while the acoustic wave propagates in the slits along the y-axis. Assuming that the working frequency f is 5000 Hz (λ=68.6 mm in air), other parameters are fixed and are in the range corresponding to the deep subwavelength wavelength in air.
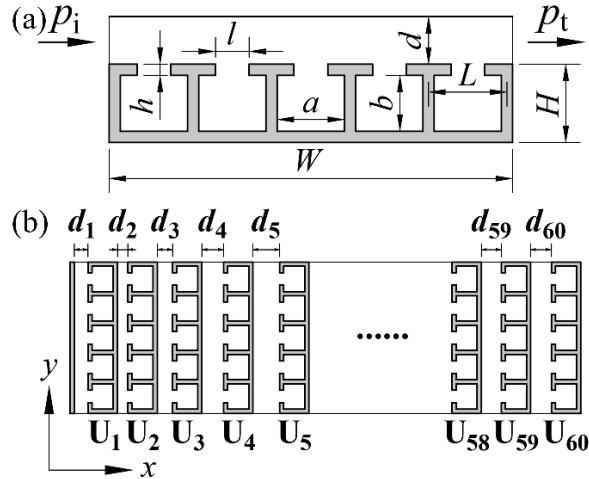

Fig. 1. (a) Schematic diagram of the elementary units of the designed AMS. (b) Schematic diagram of the designed AMS formed by arranging 60 pieces of AMS units with corresponding slit width distribution (this will be introduced later).

The HR-based AMS is based on adjusting and controlling the effective modulus

E_{eff} by varying the slit width d of the AMS unit, which can be expressed as: [37]

$$\frac{1}{E_{eff}} = \frac{1}{E_0}(1 - \frac{F\omega_0^2}{\omega^2 - \omega_0^2 - j\Gamma\omega}),\tag{1}$$

where $E_0 = \rho_0 c_0^2$ is the Young's modulus of air and $F = S_{HR}/S_{slit} = ab/Ld$ is a geometrical factor. ω_0 is the resonant angular frequency of the HR which is given by $\omega_0 = 1/\sqrt{C_{HR}M_{HR}}$, where $C_{HR} = ab/\rho_0 c_0^2$ and $M_{HR} = \rho_0 h_{eff}/l$. The resonant frequency of the HR is $f_0 = \omega_0/2\pi = 7013$ Hz. In consideration of the correction to the neck length associated with end effects, h_{eff} is the effective length of the neck of the HR, which can be expressed as $h_{eff} = h + 8l/3\pi$ [38]. Γ is the dissipation loss in the HR elements. Phase shift ϕ of the incident acoustic wave throughout the AMS could be expressed as $\phi = \omega W/c_{eff}$, where $c_{eff} = \sqrt{E_{eff}/\rho_0}$ is the effective velocity of the acoustic wave throughout the AMS without dissipation loss [16]. Hence, ϕ could be expressed as a function of d as below:

$$\phi(d) = \frac{\omega W}{c_0}\sqrt{1 + \frac{\omega_0^2}{\omega_0^2 - \omega^2}\frac{ab}{Ld}},\tag{2}$$

which shows the relationship between the phase shift ϕ and the slit width d ($d > 0$) shown as the red dashed curve in Fig. 2(a). Based on eq. (2), it can be inferred that the slit width d plays the dominant role in determining the value of phase shift ϕ. In order to compare our designed AMS with previous study [16] in which the AMS is formed by 4 HRs, the $\phi(d)$ of the 4HRs-AMS is also shown as the red dashed curve in Fig. 2(b). The phase shift curve of AMS with 4 HRs cannot cover full phase range within the working slit width range [2.3 to 4.5 mm ($0.047 \leq d/\lambda \leq 0.092$), cf. the grey region in Fig. 2(b)].

With regard to the resolution of the AMS along the x-axis, the size of the AMS unit along the x-axis should be reduced as much as possible. The smaller the size of the AMS unit, the smaller d is required. Thus, the slit width from 1.504 to 9.052 mm (corresponding to deep subwavelength of $0.022 \leq d/\lambda \leq 0.132$) is selected to realize the phase shift of AMS units over the range of 2π [cf. the grey region in Fig. 2(a)]. The

numerical simulation throughout this paper is carried out by the FEM with commercial software COMSOL Multiphysics. The material of AMS is aluminium (ρ_{Al}=2700 kg/m^3, c_{Al}=6260 m/s), while the background material of the simulation models is air at 20 degrees Centigrade (ρ_0=1.21 kg/m^3, c_0=343 m/s). The periphery of the incident and transmitted field is surrounded by perfect matched layers (PMLs) to avoid unwanted reflection. Air viscosity is ignored in the numerical simulation because the thickness of the viscosity boundary layer δ_{visc} is small enough [11]. δ_{visc} can be expressed as $\delta_{visc} = \sqrt{2\mu / \omega\rho_0}$, where μ is the dynamic viscosity which is a measure of a fluid's resistance to shearing, ω is the angular frequency and the ρ_0 is the equilibrium density. In this paper, μ=1.983 × 10^{-5} Pa·s, ω=31416 rad/s, and ρ_0= 1.21 kg/m^3. Thus, the δ_{visc} in our simulation is 2.284 × 10^{-5} m, which is four orders smaller than the wavelength for the simulated sound fields of 5000 Hz (λ=68.6 mm) and is two orders smaller than the smallest slit width (d_{min}=1.5 mm). Besides, the f/f_0 in the numerical simulation is 0.713. The f/f_0 in the numerical simulation is far away from the range $f/f_0 >$ ca. 0.78 in which the influence of resonance causes the transmission efficiency fall sharply to zero [this will be discussed below and is shown in Fig. 2(b)]. Thus, the working frequency and the resonant frequency are different enough to ignore the air viscosity from resonance in this study.

Transmission efficiency is a key aspect in the design of an AMS for acoustic focusing. The value of the slit width d directly influences the interface between the AMS unit and the air. It is crucial to keep the impedance matched, which affects the transmission efficiency of the AMS. For this reason, the transmission efficiency of the AMS unit is checked in the numerical simulation and is shown as the blue solid curve in Fig. 2(a), which illustrates the relative high transmission efficiency above 0.8 with d varying from 1.504 to 9.052 mm (0.022λ to 0.132λ). The transmission efficiency of the 4HRs-AMS unit is also shown as the blue curve in Fig. 2(b), which is relative high over the working slit width range (0.047 $\leq d/\lambda \leq$ 0.092). To further investigate the frequency response of the transmission efficiency, the transmission efficiency as a function of the frequency for the AMS units with 16 different slit widths (from 1.5 to 9.0 mm) are

shown in Fig. 2(c). The step width of the frequency varying from $f_0/2$ to f_0 is 2 Hz for the simulation of the energy transmittance of the AMS units with different slit widths. The transmission spectra show that the transmission spectra show that the transmission efficiency falls sharply to zero at smaller f/f_0 as slit width d decreases, owing to the influence of resonance. The transmission efficiency is relatively high over a relatively broad frequency range ($0.60 \leq f/f_0 \leq 0.73$), which indicates that impedance matching can be achieved in this frequency range.
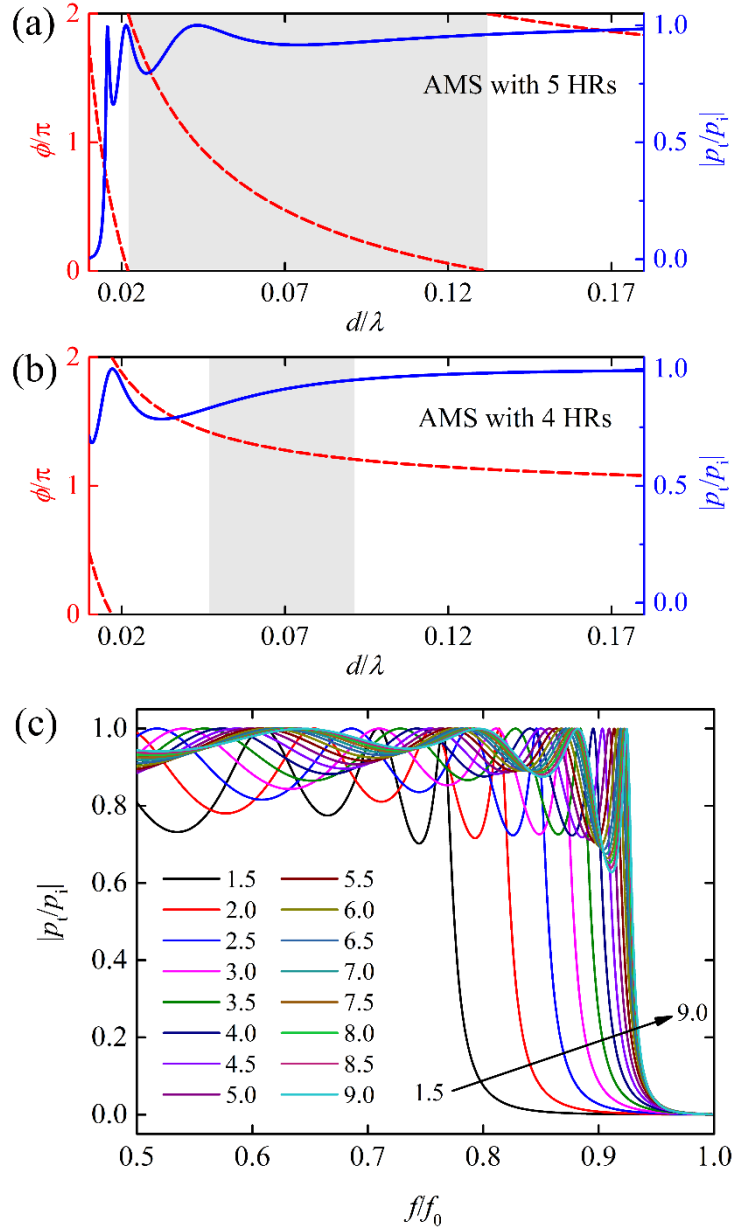

Fig. 2. (a) The phase shift ϕ (red dashed curve) and transmission efficiency $|p_t/p_i|$ (blue solid curve) of the designed AMS as a function of the slit width d. (b) The phase shift ϕ (red dashed curve) and transmission efficiency $|p_t/p_i|$ (blue solid curve) of the AMS

with 4 HRs as a function of the slit width d. (c) The transmission efficiency as a function of the frequency for the AMS units with 16 different slit widths (from 1.5 to 9.0 mm).

To examine the performance of the designed gradient HR-based AMSs, they are used to redirect the wavefront of an acoustic plane wave to focus at a designed focus point, which can be subdivided into four cases of focusing parameters. By means of the discontinuous local phase shift along the x-axis in the suitable range of deep subwavelength, it is easy to shape the wavefront for forming a desired transmission field using the designed AMS. According to the generalized Snell's law, the transmitted wave through the AMS with incident angle distribution $\theta_i(x)$ and refraction angle distribution $\theta_t(x)$ could be expressed as: [29, 39]

$$\frac{1}{k_0}\frac{\mathrm{d}\phi(x)}{\mathrm{d}x} = \sin\theta_i(x) - \sin\theta_t(x), \tag{3}$$

where $k_0 = \omega/c_0$ and $\phi(x)$ are the wave factor of air and the PSD along the x-axis, respectively.

As shown in Fig. 3, the acoustic plane wave propagates in the direction perpendicular to the surface of the gradient AMS and focuses at the designed focal length y_t of 0.3 m (4.37λ) in the first case, named as AMS-x1-y1. The designed focal point is then moved longitudinally to 0.15 m (2.19λ) and transversely to 0.2 m (2.92λ), which are named as AMS-x1-y2 and AMS-x2-y1, respectively. For the last case of nonzero incident angle [i.e. $\theta_i(x)$=30 deg] named as AMS-x1-y1-30º. For the four cases, $\sin\theta_i(x) = \sin\theta_i$ and $\sin\theta_t(x) = -(x-x_t)/\sqrt{(x-x_t)^2 + y_t^2}$, where x_t is the transverse position of the focal point. Thus, the $\phi(x)$ is derived by integrating eq. (3) as:

$$\phi(x) = -\frac{\omega}{c_0}[\sqrt{(x-x_t)^2 + y_t^2} + x\sin\theta_i] + \phi_0, \tag{4}$$

where y_t and ϕ_0 are the focal length and the integration constant of the indefinite integral, respectively. The total length of the AMS along the x-axis is less than 0.8 m (11.66λ) with 60 corresponding units to form the whole AMS.
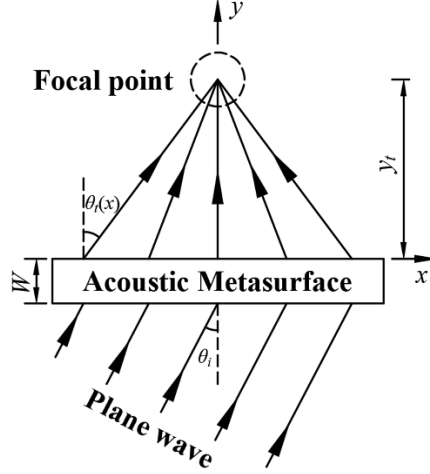
Fig. 3. Schematic diagram of focus plane wave with gradient HR-based acoustic metasurfaces. Note that θ_i, θ_t and y_t are incident angle, refracted angle and focal length, respectively.

Fig. 4(a) illustrates the PSD over a 0–2π range for the ideal metasurface (grey solid line) and the gradient metasurface (red line segments) of AMS-$x1$-$y1$ with ϕ_0 equal to 28.786 rad. The distributions of the gradient metasurface are designed using a numerical method with eq. (2) and eq. (4), which makes the midpoints of the slits along x-axis meet the ideal phase shift desired. Considering that the x positions of the midpoints of the slits not only have connections with the slit widths but also have functional relations with the phase shifts, the midpoints cannot be obtained by directly solving eq. (2) and eq. (4). Thus, we used a numerical method (Newton's iterative method) to calculate the slit width distributions of the designed AMSs. The numerical method ensures that the slit widths of our designed AMS equal to those of the ideal AMS in terms of PSD [the closeness can be seen in Fig. 4(a)] in the four significant figures. It is apparent that the shifted phase of each AMS unit meets the ideal phase shift distribution precisely and the corresponding systematic error is quite small, as shown in Fig 4(a). The normalized pressure field [cf. Fig. 4(b)] of AMS-$x1$-$y1$ reveals the phase shift ability to redirect the wavefront towards the focal point. The pressure fields around the focal point show clear circular fringes as the pattern of a point source, which illustrates the perfect focusing by the designed AMS. The normalized acoustic intensity field of AMS-$x1$-$y1$ is shown in Fig 4(c). The corresponding full width at half

maximum (FWHM) of the acoustic intensity of the focal size is shown at the upper right corner. Moreover, the energy amplification factor of the focal point $|p_{fp}/p_i|^2$ is shown below the FWHM, where p_{fp} is the pressure at the focal point. It is obvious that AMS-$x1$-$y1$ is capable of focusing the plane acoustic wave into a designed focal point. The FWHM of AMS-$x1$-$y1$ is 0.517λ which is smaller than one wavelength. Benefitting both from the high transmission efficiency and the fine discrete resolution, the acoustic intensity at the focal point of AMS-$x1$-$y1$ reaches 14.6 times larger than that of the incident wave.
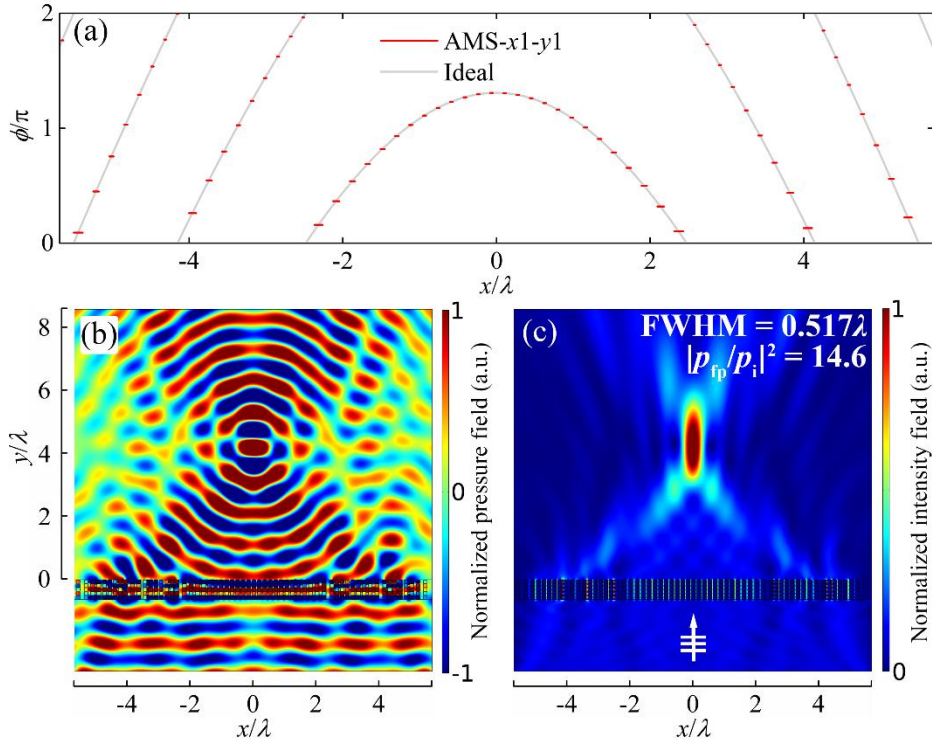

Fig. 4. (a) Ideal and actual PSD, (b) normalized pressure field, and (c) normalized acoustic intensity field of AMS-$x1$-$y1$. The FWHM of the acoustic intensity of the focal size and the energy amplification factor of the focal point $|p_{fp}/p_i|^2$ are shown at the upper right corner of the corresponding acoustic intensity field.

For a near-field focusing, Fig. 5(a) exhibits the PSD for the ideal metasurface (grey solid line) and the gradient metasurface (red line segments) of AMS-$x1$-$y2$ with ϕ_0 equal to 15.000 rad. The slope of the phase shift curve of AMS-$x1$-$y2$ is larger than that of AMS-$x1$-$y1$, which makes it feasible for ϕ_0 to be enlarged to guarantee that the length of the AMS remains almost unchanged. The normalized pressure field [cf. Fig. 5(b)]

shows that the acoustic plane wave can be focused in the near-field by AMS-$x1$-$y2$. The normalized acoustic intensity field of AMS-$x1$-$y2$ is shown in Fig 5(c) with its FWHM and $|p_{fp}/p_i|^2$ at the upper right corner. The FWHM is 0.392λ which is smaller than the Rayleigh diffraction limit of 0.5λ. The $|p_{fp}/p_i|^2$ reaches 17.6 and is significantly higher than that of AMS-$x1$-$y1$ since the acoustic wave attenuate less in near-field. Comparing AMS-$x1$-$y2$ with AMS-$x1$-$y1$, their PSD and ϕ_0 are different, while their AMS lengths are almost the same. This means that the designed AMS could shift its focal point longitudinally by rearranging the distribution of the AMS units according to eq. (2) and (4) without replacing the AMS with a new one.
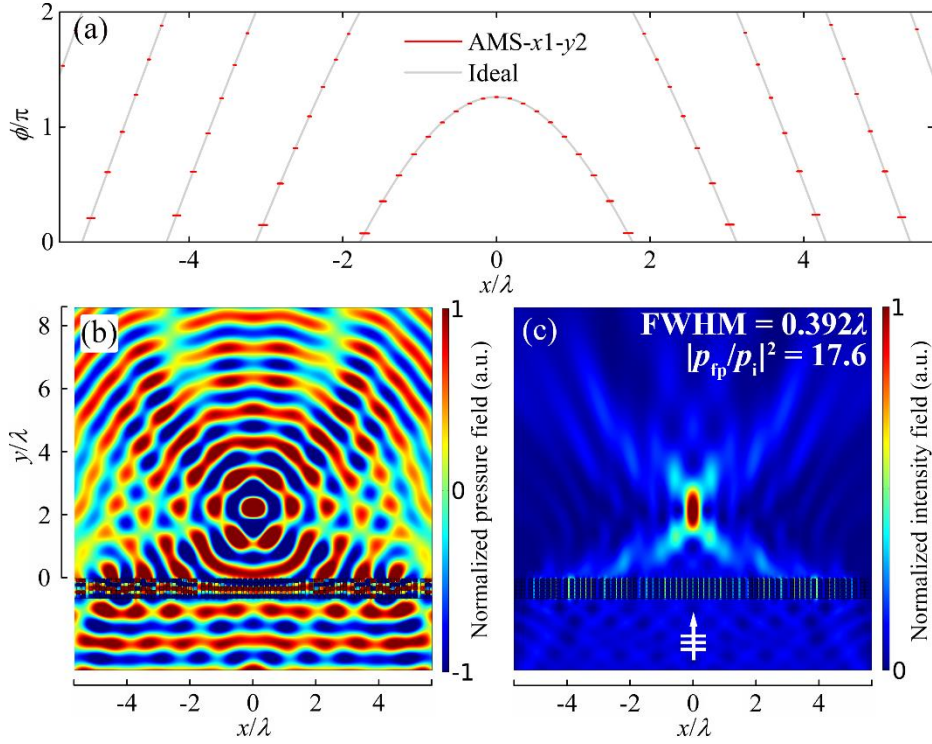

Fig. 5. (a) Ideal and actual PSD, (b) normalized pressure field, and (c) normalized acoustic intensity field of AMS-$x1$-$y2$. The FWHM of the acoustic intensity of the focal size and the energy amplification factor of the focal point $|p_{fp}/p_i|^2$ are shown at the upper right corner of the corresponding acoustic intensity field.

In the case of paraxial acoustic focusing, Fig. 6(a) illustrates the PSD for the ideal metasurface (grey solid line) and the gradient metasurface (red line segment) of AMS-$x2$-$y1$ with ϕ_0 equal to 34.579 rad. The phase shift curve of AMS-$x2$-$y1$ is the transverse shift of that of AMS-$x1$-$y1$. The normalized pressure field [cf. Fig. 6(b)] indicates that

the acoustic plane wave can be focused at a paraxial point by AMS-x2-y1. The normalized acoustic intensity field of AMS-x2-y1 is shown in Fig 6(c) with its FWHM and $|p_{fp}/p_i|^2$ at the upper right corner. It should be noted that the major-axial direction of the elliptical spot at the focal point is not parallel with the y-axis. However, the angular bisector of the angle composed of the left end point of the AMS, the focal point and the right end point of the AMS. The FWHM is 0.558λ which is slightly larger than that of AMS-x1-y1. The $|p_{fp}/p_i|^2$ reaches 13.2 and is slightly lower than that of AMS-x1-y1.
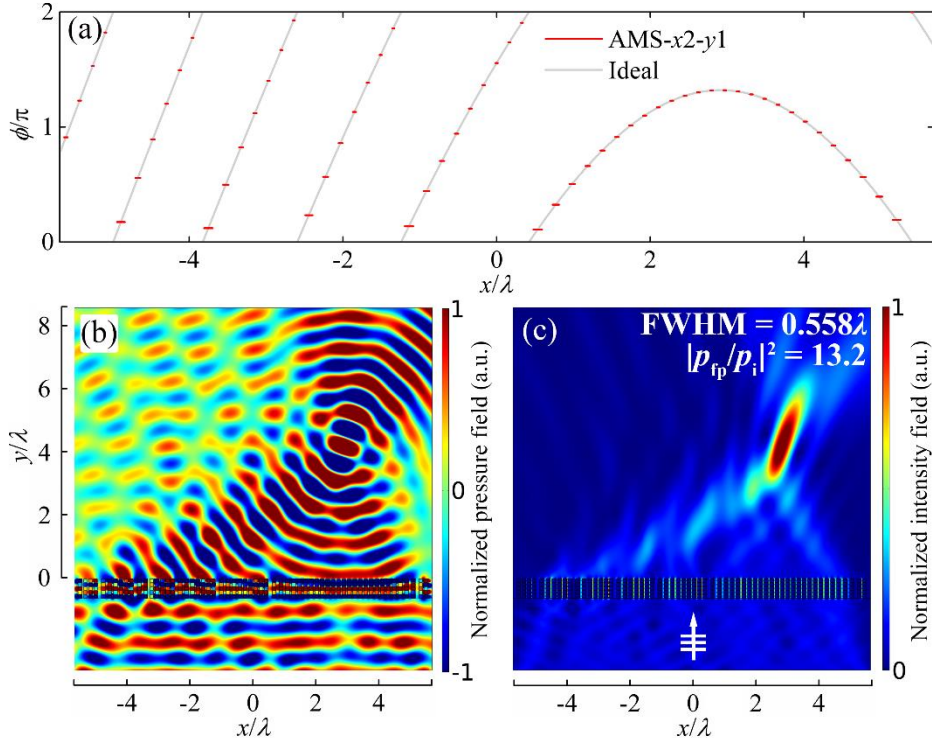

Fig. 6. (a) Ideal and actual PSD, (b) normalized pressure field, and (c) normalized acoustic intensity field of AMS-x2-y1. The FWHM of the acoustic intensity of the focal size and the energy amplification factor of the focal point $|p_{fp}/p_i|^2$ are shown at the upper right corner of the corresponding acoustic intensity field.

For a plane wave focusing with oblique incidence (θ_i=30º), Fig. 7(a) shows the PSD for the ideal metasurface (grey solid line) and the gradient metasurface (red line segments) of AMS-x1-y1-30º with ϕ_0 equal to 27.770 rad (a plane wave focusing with large oblique incidence angle θ_i=60º can be found in Supplementary S1). Compared with the bilaterally symmetrical PSDs of the other three AMS, the PSD of AMS-x1-y1-30º is not bilaterally symmetrical about the y-axis at the focal point. The incident angle

creates a linear phase difference along the x-axis. The normalized pressure field [cf. Fig. 7(b)] indicates that the acoustic plane wave can be focused in the near-field by AMS-x1-y1-30º. The normalized acoustic intensity field of AMS-x1-y1-30º is shown in Fig 7(c) with its FWHM and $|p_{fp}/p_i|^2$ displayed at the upper right corner. The FWHM is 0.497λ which is smaller than the Rayleigh diffraction limit of 0.5λ. The $|p_{fp}/p_i|^2$ reaches 12.3 and is significantly lower than that of AMS-x1-y1. This variation of $|p_{fp}/p_i|^2$ is predictable because the actual area where the plane wave impinges on the AMS-x1-y1-30º is smaller than that of AMS-x1-y1. Furthermore, the ratio of the actual area of AMS with incident angle at θ_i to that of AMS with the normal incidence is $\cos\theta_i$. Similarly, the $|p_{fp}/p_i|^2$ of AMS-x1-y1-30º can be derived as:

$$\left| p_{fp} / p_i \right|^2_{AMS-x-y-\theta_i} = \left| p_{fp} / p_i \right|^2_{AMS-x-y} \cdot \cos\theta_i . \tag{5}$$

According to eq. (5), the $|p_{fp}/p_i|^2$ of AMS-x1-y1-30º equals to 12.6, which is close enough to 12.3 to the results of the FEM.
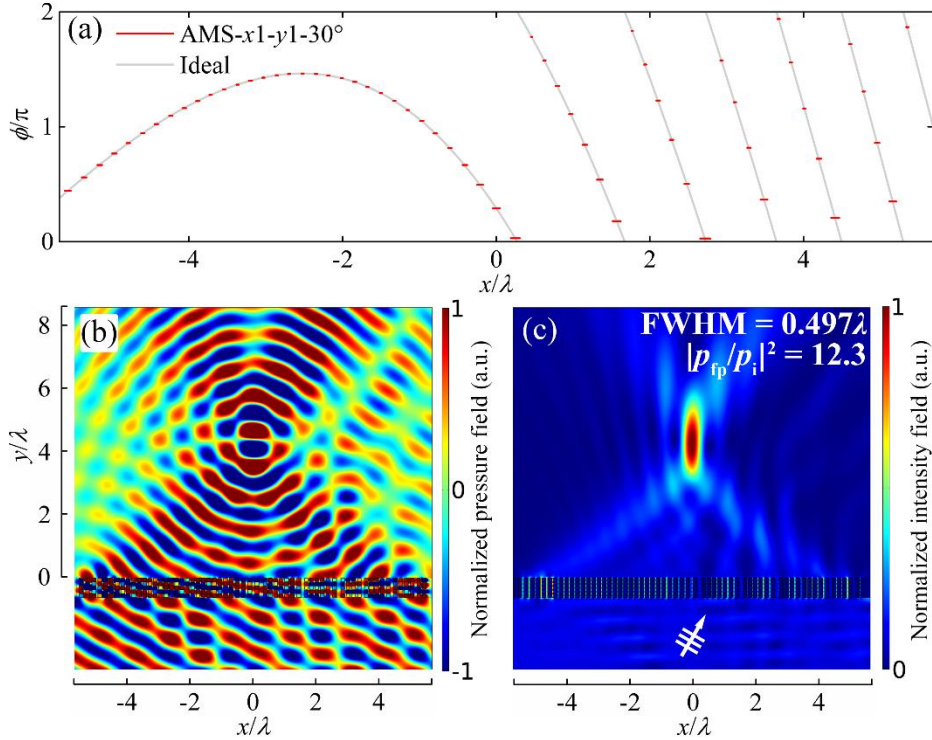

Fig. 7. (a) Ideal and actual PSD, (b) normalized pressure field, and (c) normalized acoustic intensity field of AMS-x1-y1-30º. The FWHM of the acoustic intensity of the focal size and the energy amplification factor of the focal point $|p_{fp}/p_i|^2$ are shown at the upper right corner of the corresponding acoustic intensity field.

To further examine whether the positions of the focal point created by the aforementioned four AMSs accurately locate at the designed point, the transverse and longitudinal acoustic intensity distributions are checked and shown in Fig. 8(a, b), respectively. The acoustic intensity curves are normalized by p_{fp} of AMS-x1-y2. Fig. 8(a) demonstrate the deep-subwavelength spatial resolution of the focal point along the x-axis. Moreover, the focal points are drawn back slightly due to the attenuation of acoustic waves along the y-axis, as shown in Fig. 8(b). However, the acoustic intensities at the designed focal points (i.e. at y1 or y2) attenuate less than 2% compared with the maximum along the y-axis, respectively. In general, the presented results provide a solid confirmation that the designed AMS formed from 60 units with the same structure can achieve perfect acoustic focusing performance subdivided into four cases of focusing parameters. The AMS with proper PSD is capable of focusing an acoustic plane wave at designed spot due to the capabilities of high transmission efficiency, full phase control, fine discrete resolution and tuneable structure.
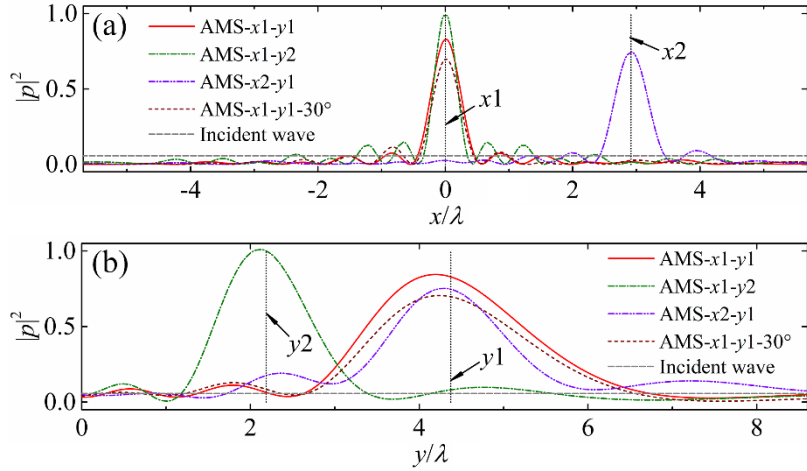

Fig. 8. Normalized acoustic intensity distribution along (m) x-axis and (n) y-axis of the AMS-x1-y1, AMS-x1-y2, AMS-x2-y1, and AMS-x1-y1-30°, respectively. The designed position of x1, x2, y1, and y2 are indicated by the black short dot.

As for transmitted acoustic focusing, one of the most important performances is the acoustic intensity at the focal point, which is represented as the energy amplification factor $|p_{fp}/p_i|^2$ in this paper. There is an inherent restriction to how much $|p_{fp}/p_i|^2$ can be increased when the AMS possesses a poor transmission efficiency or some of the AMS

units are out of phase. Because HR does not use standing waves to create resonance, thus the dimension of each element of an HR can be made to reach subwavelength scales [37]. It has been proved that the transmission efficiency of the structure of daisy-chained slits with five HRs can reach a high level near the resonant frequency as shown in Fig 2(a) and 2(b). Owing to the high transmission efficiency and the fine discrete resolution of phase shift, the $|p_{fp}/p_i|^2$ of the four aforementioned AMSs in this paper reaches 12.3 to 17.6, which are considerably high compared with those in previous studies [14, 16].

The extent of the energy concentration of the transmitted acoustic focusing can be characterized by the transverse FWHM of the acoustic intensity of the focal point. Traditional PTs have been extensively used to form ultrasonic arrays for non-destructive evaluation [7]. However, the focal resolution of the acoustic focusing created with traditional PTs is usually low, whose FWHM is much larger than one wavelength [8]. All of these FWHM in this paper are smaller than one wavelength, which is considerably smaller than the focal size formed by using traditional PTs. It is noteworthy that the FWHMs of AMS-x1-y2 and AMS-x1-y1-30º are smaller than the Rayleigh diffraction limit of conventional acoustic instruments (0.5λ), which is quite close to the FWHM of the focal point created with planar metasurface transducer [8]. As a result, the AMS proposed in this paper is likely an alternative way to improve the resolution to meet the requirements of high precision acoustic focusing.

It is common that conventional AMSs in previous studies are composed of several units with gradient phase shift performance over a 2π range. In brief, the different elementary units are arranged along the x-axis according to the phase profile to constitute the designed PSD. However, if the position of the desired focal point needs to be changed, there is no choice but to replace the AMS with a new one or to simultaneously move the AMS and the acoustic source, which presents an obstacle for further applications of AMSs. Here, the designed AMSs in this paper introduce a hybrid structure which consist of five HRs and a width-tuneable slit. In an AMS unit, the five HRs are constituted by a fixed elementary structure. On the other hand, the slit width is tuneable and depends on the distance of the two adjacent elementary structures. In

addition, the total widths of the designed AMSs can be kept close to a constant value by varying ϕ_0 in eq. (4). These characteristics make it feasible for the designed AMS to contain only one type of elementary structure and be controlled by adjusting the slit width distribution to achieve the desired PSD without replacement or movement of AMS (a more detailed explanation can be found in Supplementary S2). The presented results show that the tuneable gradient HR-based AMS is an implementation of a strategy to design tuneable acoustic lens that will be useful in medical sonography, localized heating, nondestructive flaw detection and particle trapping.

3. Conclusions

In summary, a gradient HR-based AMS was designed and realized with a series of parallel daisy-chained slits with five HRs, which is tuneable to shape an acoustic plane wave with different incident angles into different designed focal points by varying the slit width between adjacent AMS units. The transmission efficiency of the AMS is relatively high, benefitting from the impedance matching. Several typical acoustic focusing cases with different focusing parameters are realized by the designed AMS. The FEM results of these focusing cases show that moving the position of the focal point or changing the incident angle can be implemented with suitable slit width distribution according to generalized Snell's law. Further analysis indicates that the discrete resolution is quite fine because of the deep-subwavelength parameters of the AMS and the slit width as well as the accuracy of the phase shift of each unit. Acoustic intensity at a focal point can reach 12.3 to 17.6 times that of the incident plane wave as a result of the high transmission efficiency. As the AMMs and the AMSs in previous studies do not possess all these significant advantages, the gradient HR-based AMS presented in this paper offers a tuneable acoustic lens that should be useful in medical sonography, localized heating, nondestructive flaw detection and particle trapping.

References

[1] Park S H, Kim S J, Kim E-K, Kim M J, Son E J and Kwak J Y 2009 Interobserver agreement in assessing the sonographic and elastographic features of malignant thyroid nodules *Am. J. Roentgenol.* **193** W416–W423

[2] Hu Z, Yang X Y, Liu Y, Sankin G N, Pua E C, Morse M A, Lyerly H K, Clay T M and Zhong P 2007 Investigation of HIFU-induced anti-tumor immunity in a murine tumor model *J. Transl. Med.* **5** 34–44

[3] Holmes C, Drinkwater B W and Wilcox P D 2005 Post-processing of the full matrix of ultrasonic transmit–receive array data for non-destructive evaluation *NDT E Int.* **38** 701–711

[4] Fan C, Caleap M, Pan M and Drinkwater B W 2014 A comparison between ultrasonic array beamforming and super resolution imaging algorithms for non-destructive evaluation *Ultrasonics* **54** 1842–1850

[5] Yoon C, Kang B J, Lee C, Kim H H and Shung K K 2014 Multi-particle trapping and manipulation by a high-frequency array transducer *Appl. Phys. Lett.* **105** 214103

[6] Marzo A and Drinkwater B W 2019 Holographic acoustic tweezers *Proc. Natl. Acad. Sci. USA* **116** 84–89

[7] Drinkwater B W and Wilcox P D 2006 Ultrasonic arrays for non-destructive evaluation: A review *NDT E Int.* **39** 525–541

[8] Zhao J, Ye H, Huang K, Chen Z N, Li D and Qiu C-W 2014 Manipulation of acoustic focusing with an active and configurable planar metasurface transducer *Sci. Rep.* **4** 6257

[9] Khorasaninejad M, Chen W T, Devlin R C, Oh J, Zhu A Y and Capasso F 2016 Metalenses at visible wavelengths Diffraction-limited focusing and subwavelength resolution imaging *Science* **352** 1190–1194

[10] Ye M, Ray V, Peng Y, Guo W and Yi Y S 2019 Linear polarization distinguishing metalens in visible wavelength *Opt. Lett.* **44** 399–402

[11] Li Y, Jiang X, Liang B, Cheng J and Zhang L 2015 Metascreen-based acoustic passive phased array *Phys. Rev. Appl.* **4** 024003

[12] Esfahlani H, Karkar S and Lissek H 2016 Acoustic carpet cloak based on an ultrathin metasurface *Phys. Rev. B* **94** 014302

[13] Faure C, Richoux O, Félix S and Pagneux V 2016 Experiments on metasurface carpet cloaking for audible acoustics *Appl. Phys. Lett.* **108** 064103

[14] Li Y, Liang B, Tao X, Zhu X and Zou X 2012 Acoustic focusing by coiling up space *Appl. Phys. Lett.* **101** 233508

[15] Tian Y, Wei Q, Cheng Y, Xu Z and Liu X 2015 Broadband manipulation of acoustic wavefronts by pentamode metasurface *Appl. Phys. Lett.* **107** 221906

[16] Lan J, Li Y, Xu Y and Liu X 2017 Manipulation of acoustic wavefront by gradient metasurface based on Helmholtz Resonators *Sci. Rep.* **7** 10587

[17] Li Y and Assouar B M 2016 Acoustic metasurface-based perfect absorber with deep subwavelength thickness *Appl. Phys. Lett.* **108** 063502

[18] Fang Y, Zhang X and Zhou J 2018 Acoustic porous metasurface for excellent sound absorption based on wave manipulation *J. Sound Vibr.* **434** 273–283

[19] Yu X, Lu Z, L Cheng and Cui F 2017 On the sound insulation of acoustic metasurface using a sub-structuring approach *J. Sound Vibr.* **401** 190–203

[20] Tang K, Qiu C, Ke M, Lu J, Ye Y and Liu Z 2014 Anomalous refraction of airborne sound through ultrathin metasurfaces *Sci. Rep.* **4** 6517

[21] Ding C, Chen H, Zhai S, Liu S and Zhao X 2015 The anomalous manipulation of acoustic waves based on planar metasurface with split hollow sphere *J. Phys. D: Appl. Phys.* **48** 045303

[22] Liu X, Zeng X, Gao D, Shen W, Wang J and Wang S 2017 Experimental realization for abnormal reflection caused by an acoustic metasurface with subwavelength apertures *J. Phys. D: Appl. Phys.* **50** 125303

[23] Wang Y B, Luo C R, Dong Y B, Zhai S L, Ding C L and Zhao X P 2019 Ultrathin broadband acoustic reflection metasurface based on meta-molecule clusters *J. Phys. D: Appl. Phys.* **52** 085601

[24] Yuan B, Cheng Y and Liu X 2015 Conversion of sound radiation pattern via

gradient acoustic metasurface with space-coiling structure *Appl. Phys. Express* **8** 027301

[25] Li Y, C. Shen, Xie Y, Li J, Wang W, Cummer S A and Jing Y 2017 Tunable asymmetric transmission via lossy acoustic metasurfaces *Phys. Rev. Lett.* **119** 035501

[26] Ward G P, Lovelock R K, Murray A R J, Hibbins A P, Sambles J R and Smith J D 2015 Boundary-layer effects on acoustic transmission through narrow slit cavities *Phys. Rev. Lett.* **115** 044302

[27] Dubois M, Shi C, Wang Y and Zhang X 2017 A thin and conformal metasurface for illusion acoustics of rapidly changing profiles *Appl. Phys. Lett.* **110** 151902

[28] Ma G, Yang M, Xiao S, Yang Z and Sheng P 2014 Acoustic metasurface with hybrid resonances *Nat. Mater.* **13** 873–878

[29] Yu N, Genevet P, Kats M A, Aieta F, Tetienne J-P, Capassp F and Gaburro Z 2011 Light Propagation with Phase Discontinuities: Generalized Laws of Reflection and Refraction *Science* **334** 333–337

[30] Xu H, Liu W, Liao Q, Xiao S, Li B, Liu N and Yu T 2019 Highly efficient asymmetric optical transmission by unbalanced excitation of surface evanescent waves in a single—layer dielectric gradient metasurface *Appl. Phys. Express* **12** 055010

[31] Liu Z, Zhang X, Mao Y, Zhu Y Y, Yang Z, Chan C T and Sheng P 2000 Locally resonant sonic materials *Science* **289** 1734

[32] Yang Z, Mei J, Yang M, Chan N H and Sheng P 2008 Membrane-type acoustic metamaterial with negative dynamic mass *Phys. Rev. Lett.* **101** 204301

[33] Fok L and Zhang X 2011 Negative acoustic index metamaterial *Phys. Rev. B* **83** 214304

[34] Liang Z and Li J 2012 Extreme acoustic metamaterial by coiling up space *Phys. Rev. Lett.* **108** 114301

[35] Park J J, Lee K J, Wright O B, Jung M K and Lee S H 2013 Giant acoustic concentration by extraordinary transmission in zero-mass metamaterials *Phys. Rev. Lett.* **110** 244302

[36] Huang T-Y, Shen C and Jing Y 2016 Membrane- and plate-type acoustic metamaterials *J. Acoust. Soc. Am.* **139** 3240

[37] Fang N, Xi D, Xu J, Ambati M, Srituravanich W, Sun C and Zhang X 2006 Ultrasonic metamaterials with negative modulus *Nat. Mater.* **5** 452–456

[38] Kinsler L E, Frey A R, Coppens A B and Sanders J V 2000 *Fundamentals of Acoustics* 4th ed. (John Wiley & Sons, Inc., New York) Vol **4** p 274

[39] Xie Y, Wang W, Chen H, Konneker A, Popa B-I and Cummer S A 2014 Wavefront modulation and subwavelength diffractive acoustics with an acoustic metasurface *Nat. Commun.* **5** 5553